Topics in Catalysis Vol. 46, Nos. 1–2, September 2007 (© 2007)
DOI: 10.1007/s11244-007-0330-8

Catalytic reactions on platinum nanofacets: bridging the size and complexity gap

Yuri Suchorski* and Wolfgang Drachsel

Chemisches Institut, Otto-von-Guericke-Universität Magdeburg, Universitätsplatz 2, Magdeburg, D-39106 Germany

In this short review we present few selected sections of our own work on the catalytic reactions as studied on a nanoscale using the field emission and field ion microscopies (FEM/FIM) and the corresponding probe-hole techniques: magnetic field ion mass separation combined with the field ion appearance energy spectroscopy (FIAES) and an atom probe with a Wien-filter ion mass selection combined with the time of flight (ToF) and coincidence analyses. We focus on the CO respectively hydrogen oxidation on Pt nanofacets present on an apex of a Pt tip that serves as a model of a single catalytic pellet of a supported catalyst. Exhibiting a heterogeneous surface formed by different orientations, like a catalyst pellet, a Pt tip can be prepared and characterized with atomic resolution. Surface reactions in such a well-defined system can be monitored with a resolution of ≤ 2 nm by FEM or FIM and the reacting species originating from few selected surface sites can be analyzed by FIAES or ToF in a probe-hole experiment. By using the single tip the usual averaging of data over at least few catalytic pellets of the common array-type model catalyst is avoided and thus a "smoothing out" of the characteristics of the single particles can be eliminated. As a result, the correlation of processes on individual nanofacets and fluctuation effects can be studied *in situ*. Until now, the FIM/FEM techniques are known to be quite successful in studying the oscillating surface reactions on Pt and Rh surfaces. In the present review we concentrate, in turn, on the local reaction kinetics in the nanosized reaction systems as mirrored by spectroscopic measurements and on the fluctuation-induced deviations from the behaviour predicted by macroscopic rate laws.

KEY WORDS: CO oxidation; H_2 oxidation; field emission microscopy; field ion microscopy; field ion appearance energy spectroscopy; time-of-fight-spectroscopy.

1. Introduction

The technical importance of heterogeneous catalysis has motivated numerous fundamental studies concerning physical and chemical properties of dispersed metals on oxidic supports. Surface science contributed essentially to these studies by revealing an atomic-level understanding of the structure-activity relationship in surface-catalyzed reactions. In particular, the catalytic behavior of nanozised metal particles may be sensitively controlled by its morphology, by the distribution of active sites or by variation of the particle size itself, interdependencies which will be addressed in this contribution by giving an overview of our field emission and field ion related microscopic and spectroscopic studies.

In last decades there has been achieved a rapid development of structure sensitive surface analytics on an atomic level as STM (scanning tunneling microscope), AFM (atomic force microscope) and related tools, which released a tremendous progress in understanding structural and electronic properties of surfaces. Unfortunately, in the case of real catalytic systems these nanoscale methods are effectively hampered, which has to do with the enormous complexity of the supported catalysts, with the poor accessibility of the intricately coupled processes on the nanosized metal particles and with the non-steady-state of kinetics in nano dimensions. To overcome these serious experimental problems different systems modeling the heterogeneous catalysts have been designed, allowing particular access to certain features of the real systems without representing their entire complexity. One of the successful approaches is the creation of arrays of the small metal particles grown on a planar oxidic support. Several strategies of preparation have been used, such as metal vapour deposition on oxide bulk crystal surfaces or on well-ordered oxidic (e.g. alumina) films as substrates for the metal cluster deposition. The quasi two-dimensional systems prepared that way can be well characterised morphologically by surface analytic techniques [1–3] and eventually subjected to an *in situ* kinetic investigation [4].

Recently, the creation of the planar arrays of Pt particles on an amorphous SiO_2 layer by electron beam lithography had been reported [5,6]. By such a preparation method not only the particle size is controlled but also the interparticle distances can be varied which are important for the interdiffusion of species between the particles, i.e. spillover processes, playing an important role in many reactions.

Despite of these and other recent considerable achievements, the atomic-scale details of catalytic processes on the supported catalysts and even on their individual nanosized metal particles are not entirely revealed. The difficulties in addressing the details of the reaction mechanisms on the single metal nanoparticles

* To whom correspondence should be addressed.
E-mail: Yuri.Suchorski@vst.uni-magdeburg.de

have primarily to do with the "averaging" operation modi of the most surface-sensitive spectroscopies: the data are averaged over an ensemble or in the best case over few catalytic pellets of the sample, thus the individual characteristic of the single particles are often "smoothed out". As a most prominent example of such a "smoothed out" effect, the local reaction-induced fluctuations can be mentioned which are mainly confined to a single few nm-small nanofacet but can lead to the severe deviation from the "mean-field" reaction kinetics [7]. The size effects related to the size-distribution of the individual particles and to those of the particular crystal planes within the each particle can also hardly be accessed with the standard surface analytic techniques. Therefore there is a strong interest to study the reactions *in situ* on an individual metal pellet of a supported catalyst or on a single aggregate of a cluster array (Fig. 1a).

Field emission based techniques, such as Field Ion Microscopy (FIM), Field Emission Microscopy (FEM) and Lithium Field Desorption (Li-FDM) Microscopy can in principle allow investigation of local reaction kinetics on an atomic-level scale. The studied sample, the apex of a field emitter tip, exhibits a heterogeneous surface formed by differently oriented nanofacets (Fig. 1b, c, [9,10]), and thus can serve as a suitable model for a catalytic particle of comparable dimensions. However, in contrast to a catalyst particle, the tip surface can be prepared reproducibly by field evaporation and subsequently characterized with atomic resolution by imaging in the FIM. This technique, as well as the FEM and Li-FDM can be used then to visualize *in situ* the catalytic reactions such as CO oxidation or NO reduction on the platinum metal nanofacets laterally resolved on the nanoscale [11–13].

Another benefit of the field emission based methods is the possibility to study the structural changes on an atomic scale caused by molecular adsorption or by the catalysed reaction itself. Reconstruction phenomena on nanofacets not accessible by other analytic techniques are well observable in FIM [14], the reaction-induced enlargement of low index planes will be demonstrated for a Pt tip in present work.

By using the probe-hole techniques the energy of the field ions of reacting entities emitted from selected surface sites can be analyzed in a retarding potential experiment (field ion appearance energy spectroscopy, FIAES), which provides the binding energy of the (neutral) atoms or molecules adsorbed on these sites. The probe-hole approach can be also applied for the mass analysis by magnetic separation or for the time of flight (ToF) measurements. The ToF analysis can also provide coincidences of different product molecules during ongoing reaction in a very narrow time window, an example will be given below. By monitoring the local work function of the apex area complementary information can be obtained which reflects the local spatial distribution of adlayers. *In situ* FIM/FEM measurements are possible at a reactive gas pressure up to some 10^{-4} mbar at temperatures up to 650 K depending on the used substrate.

Analysing the different systems emulating the behaviour of the supported catalysts Prof. K. Hayek had pointed out the necessity to consider the effect of the electric field arising from the Schottky-like barrier at the metal-oxide interface [15]. The field strength depending on the difference between the Fermi levels of metal and support and influenced by the degree of electronic charge screening may range in the V/nm range. For experimental simulation such a field can hardly be applied externally in real systems, but in case of a tip apex it is easy to apply the necessary field of the desired strength (in the range 0–40 V/nm, limited by the field evaporation of the probed metal solely) and polarity.

In the following short review on our own work we will demonstrate the capability of the field emission based microscopies (FEM/FIM) and of the (often underestimated) spectroscopies (TOF, FIAES) applied to the CO respectively hydrogen oxidation on platinum nanofacets. The FIM allowed first direct atomic scale observation of reactive sites during the ongoing reaction [16] and was quite successful so far in studying the oscillating surface reactions on Pt and Rh surfaces [17,18], the summary of corresponding studies can be found in the recent comprehensive review [19]. We focus in turn in the present contribution on the local reaction kinetics in the nanosized reaction systems reflected mainly by spectroscopic measurements and on the fluctuation-induced deviations from the behaviour predicted by macroscopic rate laws.

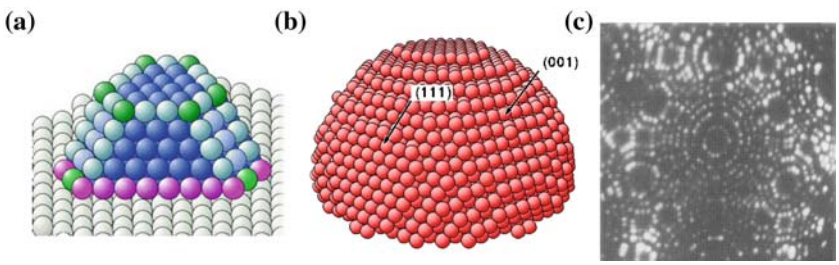

Figure 1. (**a**) Metal aggregate on an oxide substrate (from [8]). (**b**) Ball model of the apex of a spherical fcc tip (from [9]) (**c**) Field ion image of the [111]-oriented Rh field emitter tip (from [10]).

2. Experimental

In situ studies of catalytic reactions were performed in three stainless steel FIM/FEM set-ups equipped with different field ion analysis techniques. The differentially pumped FIM/FEM ultra high vacuum (UHV) chambers were run as constant flow reactors by admitting the purified (liquid N_2 baffle) reactive gases to the Pt sample via leak valves from constant pressure (Baratron controlled) reservoirs. The pressure in the UHV chambers as well in the gas supply system was monitored by spinning ball gauges to avoid effects from hot filaments. The instruments could be operated either in the FEM mode, what means, that due to the applied negative field (<5 V/nm) tunneling electrons monitor the local work function of the tip apex area, or in the FIM mode where a positive field ($\sim 10-40$ V/nm) is applied providing the field ionization of adsorbed species. The emitted field ions map then the surface location of their formation. In both modes the radial emission of the electrons/ions provides a projected magnified ($\sim 10^6$) map of the apex area on the image intensifier some cm away (projection microscope). The well studied details of the FIM/FEM imaging processes are comprehensively described in the literature [20] including the use of the reactive gases as imaging species [21].

The Pt specimens were prepared as sharp tips with an apex curvature of about 100 nm by electronically controlled electrochemical etching [22], cleaned in the FIM by field evaporation and characterized with atomic resolution by Ne^+ FIM imaging. For further analysis of the locally emitted field ions two versions of the probe-hole techniques were used: (i) magnetic field mass separation combined with retarding potential analysis (Figure 2), and (ii), an atom probe with a Wien-filter ion mass selection combined with the coincidence analysis (Figure 3). Spectroscopic data were collected by a multichannel analyzer connected to computer aided data acquisition system.

2.1. Field ion appearance energy spectroscopy

By measuring the onset of the field ion energy distribution one can derive thermodynamic information about the energetics of field ionization processes at the surface as was shown in early experiments by Müller and Bahadur [23]. In our set-up the local Field Ion Appearance Energy Spectroscopy (FIAES) was performed by probe-hole selection of field ions originated from the surface sites of interest. The selected ions are directed to the entrance of a focussing lens (Fig. 2a, pos.1), the collimated ions then pass a 60° magnetic sector field for mass-to-charge separation and are analysed finally in the retarding potential analyser. The current of ions reaching the single particle detector is measured as a function of the voltage δ, applied between retarder electrode and emitter to vary the height of the retarding electrostatic barrier. The appearance energy A, as was introduced by Goldenfeld et al. [24], is derived for a singly charged ion:

$$A = \Phi_{ret} - e\delta^{on}, \tag{2.1}$$

where ϕ_{ret} is the work function of the retarder, e is the charge of the ion and δ^{on} is the onset voltage for ion collection. In principle A is the energy to remove an electron of a given molecule (ground state) to create an ion at its surface position. By conducting a closed thermionic cycle the appearance energy for a field desorbed molecule amounts [25]:

$$A = I + H(F_{loc}) - Q(F_{loc}) \tag{2.2}$$

if temperature dependent terms are neglected. In this expression I means the ionisation potential of the molecule, $H(F_{loc})$ means the adsorption energy at the local field, and $Q(F_{loc})$ is the activation energy for field desorption of this species. An extended discussion of the energy terms involved in field ion appearance spectroscopic measurements is given in references [21,26]. For field ionisation of a noble gas atom like Ar the field dependent terms do not contribute essentially at elevated temperatures, so that according to $A = I = \phi_{ret} - e\delta^{on}$ the work function of the retarder can be determined from the known ionisation potential. In case of reactive gases, such as e.g. CO, typical retardation curve exhibit shapes shown in Figure 2b [27]. Using equation (2.1) and (2.2) the field dependence of $H(F)$-$Q(F)$ can be obtained from the measured δ^{on} values (Fig. 2c). From the temperature dependence of the CO^+ and O_2^+ ion rate a maximum value for Q of only 0.1 eV has been estimated, so that ordinate in Figure 2c mainly represents the binding energy of the CO and O_2 in the chemisorbed state at the local field conditions. This procedure can be repeated for any reactive gas ions and can also be used during a reaction to provide *in situ* data about the binding energy of the reactants (see discussion in chapter 3.2).

2.2. Laser pulsed atom probe

In the laser pulsed atom probe (Figure 3) a probe hole in the channel plate-screen detector selects, similarly as in the FIAES, the ions originating from the region of interest on the apex area. These are focussed then into the entrance of a Wien-filter (crossed electrostatic and magnetic fields, both perpendicular to the ion trajectory) [28,29]. The mass-to-charge selected ions can be directed to different parts of a dual channel plate detector and registered independently as single events. By this, correlation of the reaction rate of different products can be derived. For identifying surface species the probe is irradiated by a pulsed laser (Nd:YAG, 10 ns pulses, 532 nm) and the corresponding ions are field desorbed due to the thermal activation [30]. Chemical identity of these ions is derived from the time of flight

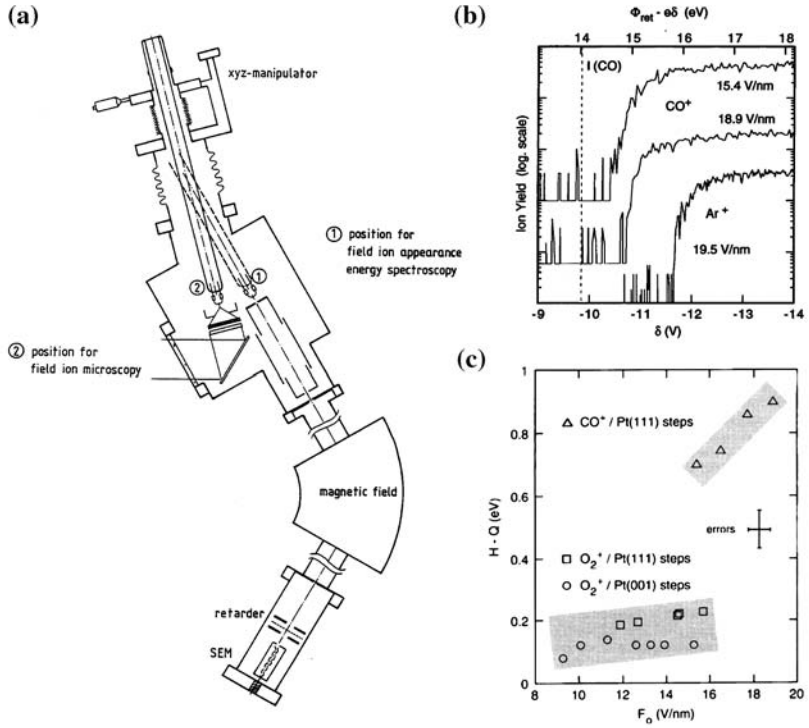

Figure 2. (**a**) FIM set-up for mass-to-charge resolved field ion retarding potential measurements (pos.1) and field ion microscopy (pos.2). (**b**) O_2^+ retardation curves measured at 11.9 V/nm from *O*-covered *Pt*(111) step sites at $T = 79$ K. The dashed line indicates the ionization energy for a free O_2 molecule. The *Ar* retardation curve used for calibration of ϕ_{ret} is also shown. (**c**) Data for *H*-*Q* as a function of applied field F_0. The upper (lower) results have been obtained from CO^+ (o_2^+) field ion appearance energies measured at 79 K for stepped Pt-surfaces covered with CO_{ad} (O_{ad}). Taken from [27].

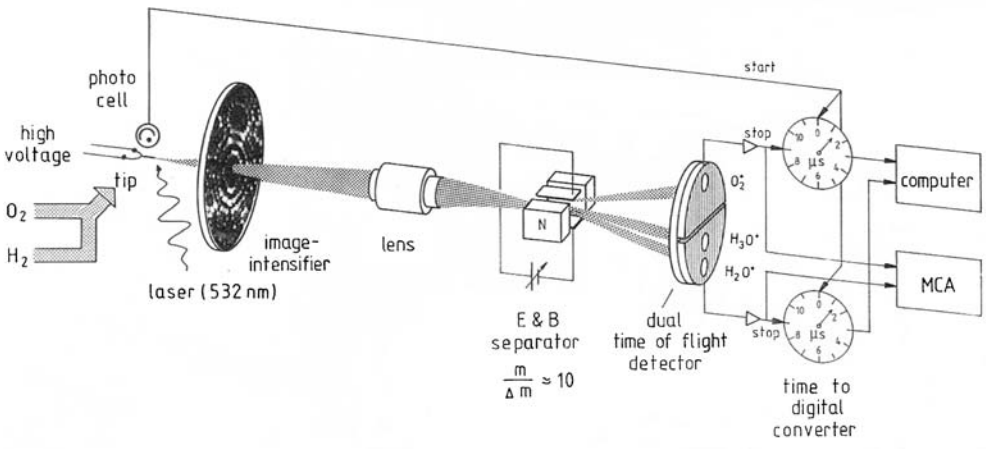

Figure 3. Scheme of the pulsed laser atom probe. Reaction gases are introduced separately at const. flow and pressure. Field ion micrographs are recorded by a CCD camera, surface species are field desorbed by pulsed laser irradiation and by TOF measurement identified, local field ion rates are mass separated by a Wien filter and recorded by a multichannel analyser, for coincidence measurements time to digital converters are started and stopped by successive events (single particle detection). Taken from [29].

(ToF) data at a tube length of 0.6 m. The used time-to-digital converters (2 ns resolution) could also be applied for deriving of the time-correlation of different product species. In this case the clock is started by the arrival of lighter ion and stopped then by the next heavier one (laser inactive).

3. Oxidation of carbon monoxide on platinum nanofacets

3.1. Reaction mechanism

Carbon monoxide oxidation has been intensively and systematically studied since Irving Langmuir [31], both over the single crystals as well as over the

supported catalysts in UHV and at elevated pressures. In elegant modulated beam studies by Engel and Ertl [32] the Langmuir-Hinselwood mechanism (LH) of the reaction was proven and is now commonly established for the CO oxidation on Pt. The LH mechanism implies the adsorption of the reacting species on the surface before the reaction itself and proceeds in the case of the CO oxidation on Pt in accord to the following steps (*means empty surface site):

$$2CO + 2* \leftrightarrow 2CO_{ad} \quad (3.1)$$

$$O_2 + 2* \leftrightarrow 2O_{ad} \quad (3.2)$$

$$CO_{ad} + O_{ad} \rightarrow CO_2 + 2* \quad (3.3)$$

In the first step CO adsorbs molecularly (adsorption/desorption equilibrium), in the second step oxygen adsorbs dissociatively (two adjacent surface sites are necessary), in the third step CO_2 is formed and leaves the surface immediately at usually used temperatures 300–600 K. The additional details of the reaction mechanism, such as the role of diffusion and lateral adsorbate–adsorbate interaction are well studied and utilized in the kinetic modelling which describes the system using the ordinary differential equations or the Monte-Carlo modelling [33–35]. The CO/O/Pt reaction system exhibits a pronounced nonlinearity which manifests itself under certain conditions in the oscillations in the reaction rate. The oscillating behaviour of CO oxidation was intensively studied using PEEM (photoemission electron microscope) on the macroscopic (~μm) scale over the many years and is well reflected in a number of reviews, where such spatial-temporal phenomena as target patterns, island formation, spirals, standing waves, etc, are described [36]. Since beginning of the nineties, it was demonstrated that such phenomena can be also imaged *in situ* with a nanometer-resolution using the Pt field emitter tips as samples, many results on such a visualization are summarized in the recent review [19]. Such a ''quantum leap'' from the μm- to the nm-scale raised questions about the compatibility of the ''nanoscale'' studies with the single crystal measurements, namely about the: (i) role of the FEM/FEM imaging process itself (influence of the applied electric field) on the reaction mechanism, (ii) influence of the structural heterogeneity of the field emitter tip surface since dynamic coupling effects between the individual planes may lead to a different behaviour than that observed in regular single crystal experiments and last but not least about the (iii) role of fluctuations on the reaction kinetics and possible fluctuation-induced deviations from the behaviour predicted by macroscopic (mean-field) rate laws.

3.2. *The role of the applied field and compatibility of the nm- and μm-scale studies*

To minimize the influence of the dynamical coupling with neighbouring planes in the revealing of the field-effects a particular tip geometry was prepared for a [111]-oriented Pt tip in a way that the {100} planes were less well developed (see insert in the Figure 4a) [37]. The reaction zone was restricted therefore to a triangular area formed by {110} planes which contribute mainly to the total field electron emission current and to the intensity of the FEM image. Since the {110} regions and adjacent vicinals trigger the transition of the whole tip surface from the inactive (CO covered) to the reactive (oxygen covered) surface via the spreading of reaction fronts, the behaviour of the {110} orientations determine, to a large degree, the results of the FEM observations.

To prove experimentally the effect of the imaging electrostatic field (~4 V nm^{-1}) on the dynamic behaviour of catalytic CO oxidation, the FEM measurements with a pulsed high-voltage supply varying the length of the duty cycles were performed [37]. No influence of the duration of the pulses on the catalytic CO oxidation was detected. This shows that the FEM results on the CO oxidation on platinum metal field emitter tips are not influenced by the imaging field and can be interpreted as quasi-field-free.

In the FEM studies the same approach as in the PEEM can be used to identify the reactive state of the sample surface. In its catalytically active state, the Pt surface is oxygen-covered and exhibits a high work function corresponding to a low emission current, whereas in its inactive (CO poisoned) state, the surface exhibits a lowered work function and thus a high emission current (and image brightness). The existence diagram for oscillations and bistability in parameter space (kinetic phase diagram or bifurcation diagram) can thus be obtained by monitoring the local field emission current (or image brightness) while adjusting of the external parameters such as p_{CO}, p_{O2} and T. Similar is valid also for FIM, where the different ionization probabilities for oxygen (used as imaging gas) over the oxygen- and CO-covered surface [38] create the image-contrast (we note that the FIM-image appears as a ''negative'' of the FEM image, that is the active surface sites emits intensively).

Figure 4a shows the kinetic phase diagrams obtained with both, FIM and FEM, for the same tip and the same oxygen partial pressure 4×10^{-4} Torr and Figure 4b illustrates the local and ''global'' oscillatory behaviour of the reaction on the tip apex shown in Figure 4a. In the FEM diagram (open triangles in the plot) the shaded area above the crossing point of the two lines defines the existence range for oscillatory behaviour in the area between the two lines below the crossing point, one obtains a simple hysteresis as one varies *T* cyclewise, i.e.

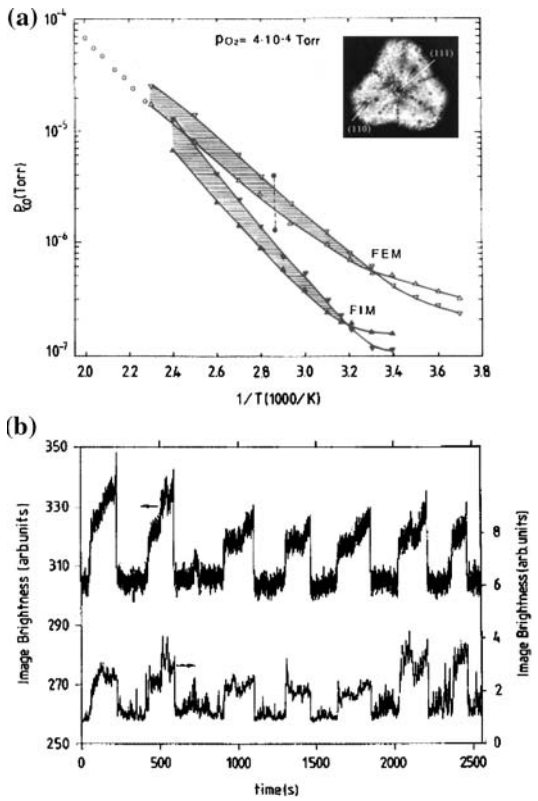

Figure 4. (**a**) Reactive phase diagrams for CO oxidation on Pt nanofacets determined with FEM (F_0 = 4 Vnm^{-1}) and FIM (F_0 = 12 Vnm^{-1}). The shaded areas mark the existence ranges for the oscillations. Below their crossing point, the boundary lines for instabilities enclose a region of bistability. The open circles are Pt(110) single crystal data indicating the existence range for oscillations [39]; the bistability range of reaction on Pt(110) at T = 349 K is indicated by filled circles [40]. The insert shows the geometry of the [111]-oriented Pt tip used in our experiments (clean Pt surface imaged at 78 K with FIM using Ne as imaging gas, F_0 = 35 Vnm^{-1}); the central (111) and one of three {110} planes are indicated. (**b**) Oscillatory behavior of CO oxidation on the Pt tip apex displayed in the insert of (**a**). Upper curve, total FEM image intensity; lower curve, local FEM intensity of the (110) plane. T = 398 K, p_{CO} = 6.2×10^{-6} Torr, p_{O2} = 4.3×10^{-4} Torr. Taken from [37].

the system is bistable (see also the Figure 5d). To the left of this area, the system is in a monostable (oxygen-covered surface) state, and to the right of this area, the surface is CO-covered. Although different facets are exhibited, the whole tip area undergoes synchronous transitions from a CO-covered to an oxygen-covered surface and vice versa at the bifurcation points of the bistability region (compare variation of the local and total image intensity in Figure 4b).

The comparison of FEM measurements with data for catalytic CO oxidation on a macroscopic Pt(110) surface reveals differences: the study by Eiswirth et al. (open circles in Figure 4a, [39]) and Moldenhauer (filled circles, [40]) suggest the position for the bifurcation point which is significantly shifted in respect to our FEM results. At elevated temperatures, the oscillating range on the Pt tip more or less follows the parameter range of dynamic instabilities on a Pt(110) plane, but the differences occur with respect to the type of instability (oscillation on the tip, bistability on the single crystal), which can be attributed to the size of the system and to dynamic coupling effects of the {110} facets with neighboring orientations.

In contrary to the FEM data, the phase diagram obtained by FIM (filled triangles in Figure 4a) where a significantly higher imaging field (12 V nm^{-1}) of the opposite polarity was applied, appeared as shifted significantly to lower p_{CO} values in comparison to the field-free one. Such a significant shift in respect to p_{CO}, and, particularly, the different plot-slopes in the FEM- and FIM-diagrams cannot be explained by the known field-induced modification of the kinetic gas flux known as the "field-compression effect" [41]. Although the known theoretical and empirical estimations [42] predict a field-induced increase in the effective pressure of CO and O_2 by roughly a factor of five at fields of 10 Vnm^{-1}, the ratio p_{O2}/p_{CO} would, however, change by a factor of less than 1.2 (because of similar polarizabilities of CO and O_2), which is far below the factor of 2–4 resulting from Figure 4a. Moreover, the single crystal data of Refs. [39,40] predict that pure field compression effect would introduce the opposite changes in the slope of the bistability region than that exhibited in Figure 4a.

To explain the field-induced effect, we employ the FIAES technique presented in chapter 2 to determine the field-dependence of the binding energy of adsorbed reactant species. According to the physical meaning of the appearance energy for field-desorbed ions, the experimentally obtained values are related to the (in general field-dependent) binding energy $H(F)$ of adparticles just before the ionization (see eq. 2.2). In Figure 2c the corresponding experimental values for the CO^+ and O_2^+ ions emitted from the few step sites of the Pt(111) nanofacet, are plotted. The plots show that the binding energy of adsorbed CO increases quite strongly with the electric field strength, whereas adsorbed O_2 displays a relatively weak dependence on the applied field, in agreement with the self-consistent calculations by Kreuzer and Wang [21].

The field effect on the binding strength of adsorbed species results from the additional charge transfer caused by a field-induced redistribution of the electronic charge at the surface: the "positive" field applied in FIM reduces the electronic density outside the geometric surface plane as compared to the field-free case [43]. The changes in the binding energies of the molecular adsorption states of O_2 and CO on Pt, shift the adsorption/desorption equilibria of the molecular O_2 species and of CO. Enhanced binding strength of CO modifies the supply rate of CO into the reaction zone whereas the considerably lower binding energy of O_2 molecules (less than 0.2 eV for the same field) leads to an insignificant additional

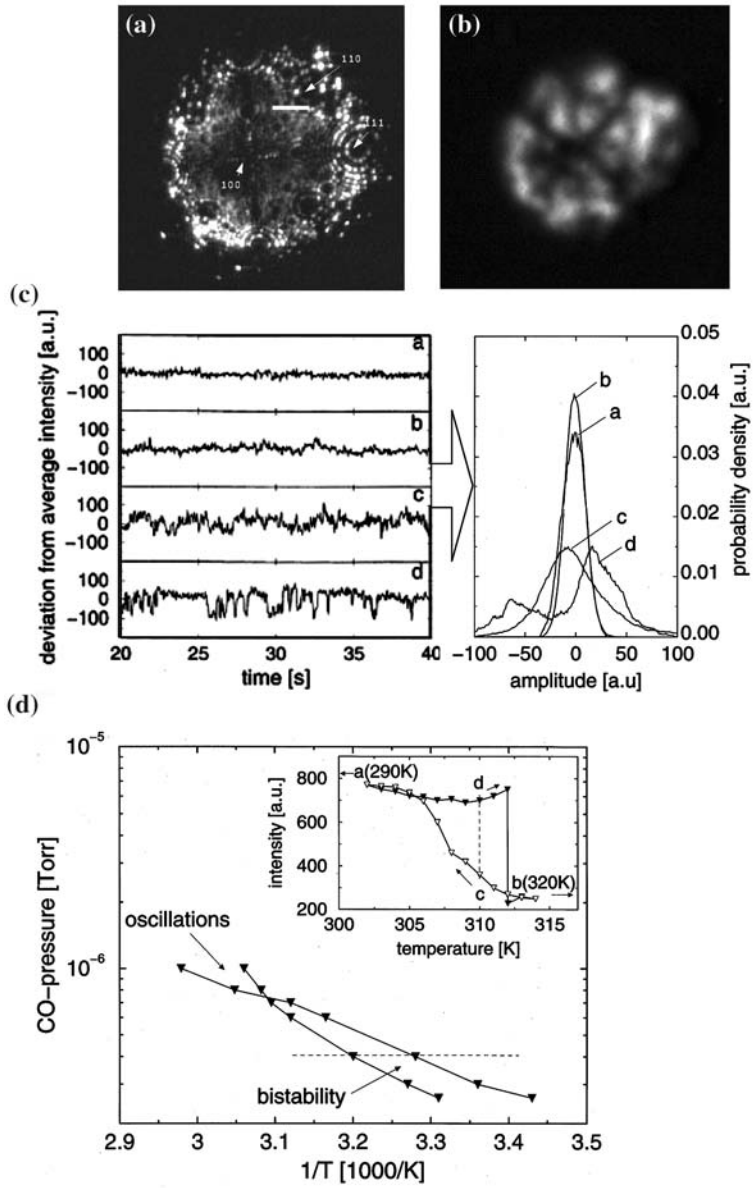

Figure 5. Fluctuation-induced transitions in catalytic CO oxidation on a Pt field emitter tip. (**a**) FIM image showing the crystallography of the [100]-oriented Pt tip (T = 78 K, imaging gas Ne, field strength F = 36 Vnm^{-1}). The rectangular window indicates the area in which fluctuations were monitored. (**b**) FEM image of the same area (same scale) but under reaction condition (T = 310 K, $p_{O2} = 4.0\times10^{-4}$ Torr, $p_{CO} = 4.0\times10^{-7}$ Torr, F = 4 Vnm^{-1}). (**c**) Time series of the local (2×2 nm^2) FEM brightness in the area marked in (**a**) and respective probability distributions (right hand side). (**d**) Reactive phase diagram obtained for the tip shown in (**a**) at constant $p_{O2} = 4.0\times10^{-4}$ Torr, the inset shows the hysteresis in local FEM brightness (2×2 nm^2) for the area marked in (**a**) upon cyclic variation of T: filled triangles, heating; empty triangles, cooling. The points *a–d* in hysteresis loop correspond to the respective curves in (**c**). Based on [7].

supply of O_2 molecules under reaction conditions. Both effects taken together lead to a shift of the FIM diagram towards the smaller p_{CO} values in comparison to the (quasi-field-free) FEM-diagram. At increasing substrate temperatures, the influence of the field-modified precursor state for CO becomes smaller, so that the FIM diagram approaches the "field-free" case, as is clearly visible in Figure 4a.

3.3. Fluctuation-induced effects

Nanofacets on the apex of a Pt field emitter tip exhibit a prime example of nanosized reaction systems where a significant influence of fluctuations is potentially expected because of the $N^{-1/2}$ scaling of the relative amplitude of fluctuations in small systems (N being the number of fluctuating particles, e.g. reacting molecules). Since the numbers of the reacting particles on such a nanofacet

varies in the 10^2–10^3 range, one may observe deviations from behaviour predicted by macroscopic rate laws, such as, e.g. fluctuation-induced transitions in a bistable system for which an infinite residence time is predicted by the mean-field theory. The "parallel" imaging principle of the FEM/FIM makes these techniques naturally suitable for monitoring fluctuations: the processes proceeding on the different surface regions can be analysed simultaneously and the time resolution is limited just by the recording speed of the used video-technique. Digitizing and sophisticated processing of the corresponding video-images allow to study the reaction dynamics within the "virtual probe-holes" (regions of interest which correspond to certain surface regions of few nm^2) arbitrarily located on the surface [44]. We employ the FIM with its atomic resolution for identifying the surface crystallography of the studied area and the FEM with its resolution of $\sim$2 nm for monitoring fluctuations on the same surface under reaction conditions (Figures 5a and 5b).

As an example, we consider the local time series recorded for a small 2×2 nm^2 window inside the area in the vicinity of the (110) facet (Figure 5a) and focus on the distinguishing fluctuation behaviour of different ranges of the reaction. The small amplitude fluctuations caused mainly by the CO diffusion and characterized by a Gaussian probability distribution were observed in the *monostable* range on the inactive branch of the reaction. This is illustrated by a time series *a* (Figure 5c left hand side) and a corresponding probability distribution (Figure 5c right hand side) registered at the point *a* in the hysteresis loop in Figure 5d. Similar time series but with somewhat higher magnitude of fluctuations were also observed in the monostable range on the active branch (curves *b* in Figure 5c, corresponding to point *b* in Figure 5d). Unexpectedly, in the *bistable* range of the reaction the probability distribution becomes broad and asymmetric and turns even into a bimodal probability distribution (curves *c* and *d* in Figure 5c, correspondingly). This bimodal distribution evidences the fluctuation-induced transitions between the two possible states in the bistability region [7]. More detailed studies using the Haar-Wavelet-Analysis detected that such fluctuation-induced transitions occurs spatially correlated over the flat facet surface (the mentioned region in the vicinity of Pt(110) was identified as a small (331) facet) [45], and are confined by the first atomic step due to the disturbed diffusional coupling over the stepped surface [46,47]. We note that this effect cannot be predicted within the mean-field theory, the Monte Carlo simulations naturally incorporating the stochastic nature of the modelled processes can, in turn, predict such an effect provided the modelled system is sufficiently small and in close proximity to a bifurcation (critical) point where bistability vanishes and fluctuations diverge [48,49].

Another unexpected result obtained by using the "virtual probe hole" was the absence of the synchronization between the fluctuations on the neighbouring facets [50]. This is unexpected because the tip is known to behave as one synchronized dynamic system during kinetic transitions from the active to inactive state (marked by lines in cross-shaped diagrams of Figure 4a and 5d) the spatial coupling occurs apparently due to the fast CO diffusion. The lack of the synchronization in respect to fluctuations between the various orientations is illustrated in Figsures 6a and 6b where the time series showing the fluctuations of the local FEM brightness for the chosen (100) and (113) facets on a [100]-oriented Pt tip are recorded simultaneously. This effect can be understood if one takes into account that differently oriented facets may own different intrinsic bifurcation diagrams at the same external p, T, parameters. The stepped regions around the individual facets disturb the diffusive coupling via CO so much that it is not sufficient to synchronize the fluctuations on different facets. Figure 6c illustrates this by showing the break in the spatial correlation of the fluctuation at the position of the first atomic step confining the individual facet. We note that within the individual facet the reaction-induced fluctuations are generally well correlated as was demonstrated by the corresponding POD- (proper orthogonal decomposition) and Haar-Wavelet-Analysis of the FEM video-sequences [45,50]. The degree of the spatial coherence increases at approaching the critical point C simultaneously with the amplitude of fluctuations (compare Figs. 6c and 6d) [49]. Similar behaviour is well known for the equilibrium systems where the correlation length diverges (in an infinite system). In our case the correlation length seems to be limited by the size of the facets.

The noise-induced transitions in the CO oxidation detected first on the Pt nanofacets allowed to explain the vanishing bistability during CO oxidation on a Pd model catalyst consisting on the small Pd particles [51]. For the model system consisting of particles of $\sim$500 nm size a pronounced bistability is observed which vanishes when the particle size becomes smaller than 6 nm (approximately the size of the individual facet of the field emitter tip). The fluctuation-induced transitions, which occur in an unsynchronized way lead to the apparent disappearance of the bistability as observed by an averaging method (total CO_2 rate for many particles was measured in Ref. [51]).

4. Hydrogen oxidation on Pt field emitter

In comparison to the CO oxidation discussed above the catalytic oxidation of hydrogen is less relevant from the technical point of view but the fact that in this case both educts have to dissociate on the catalyst implies a higher number of reaction steps and eventually different

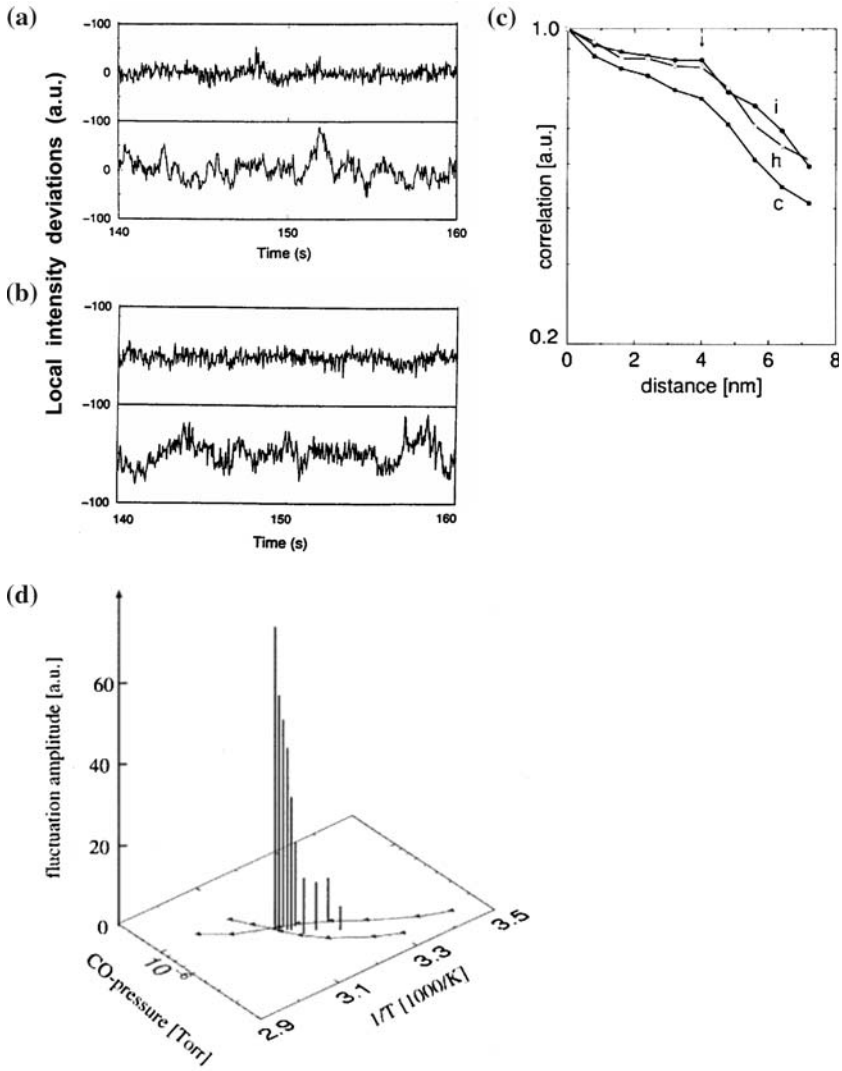

Figure 6. Fluctuations during catalytic CO oxidation on different facets of a Pt tip. (**a**) The local time series for a (100) facet recorded for the points d (upper curve) and c (lower curve) of the hysteresis loop in Fig.5d (from [50]). (**b**) The same as in (**a**) but recorded simultaneously for a (113) facet of the same tip. Time series in (**a**) and (**b**) are not synchronized despite of the diffusive CO coupling (from [50]). (**c**) Break of the spatial correlation of the first atomic step (marked by an arrow) confining the individual (112) facet. The letters refer to different reaction conditions. The distance zero refers to the opposite atomic step (edge of the facet). Taken from [49]. (**d**) Increase in the average amplitude of the local FEM brightness fluctuations on a Pt(112) facet at approaching the critical point given by the crossing point of the two boundary lines of the bistability range (from [49]).

reaction pathways. It is tempting to study this reaction by field ion microscopy especially as the product molecular water is directly acting as imaging gas [52], thus providing direct access to the reaction sites.

4.1. Reaction kinetics

Since 1822, when Döbereiner discovered the cold combustion of hydrogen by dispersed platinum, the kinetics of the hydrogen-oxygen reaction has been studied by many groups (see a comprehensive review by Norton [53]). There is a general agreement that after dissociative adsorption of H_2 and O_2 the reaction follows a LH-mechanism according to the main steps (4.1) to (4.3):

$$H_{ad} + O_{ad} \leftrightarrow OH_{ad} + * \tag{4.1}$$

$$H_{ad} + OH_{ad} \rightarrow H_2O_{ad} + * \tag{4.2}$$

$$OH_{ad} + OH_{ad} \rightarrow H_2O_{ad} + O_{ad} \tag{4.3}$$

The reaction starts near 120 K on Pt [54], which is well below the desorption temperature of water at 180 K. At

higher temperatures, H_2O desorbs from an equilibrated state indicated by a cosine-angular distribution of the desorbing molecules [55]. On Pt, the reaction has been studied in the limit of low coverages [56] as well in the limit of high coverages [57], where the interaction of adjacent adspecies shifts the activation energy to lower values.

The hydrogen oxidation on Pt was visualised by FIM and FEM for first time in the former group of Block in Berlin [22, 52, 58, 59] later the FIAES was also applied [60,61]. The imaging process in FIM is governed mainly by the ionisation potential I of the impinging molecule (field ionisation) or by the appearance energy A if the molecule is adsorbed (field desorption), the lower these values the higher (exponentially) the field ion rate is [62]. In this context it seems, by comparing the educts (I_{O2} = 12.1 eV, I_{H2} = 15.4 eV) and the product (I_{H2O} = 12.6 eV) that the oxygen field ionisation rate should prevail. Otherwise it is known from early field desorption experiments [63,64] that in this case the species H_3O^+ dominate in the field ion current. The reason for this stems from the low appearance energy value of only 10.4 eV for this species [61]. For clarification a "flash desorption" was performed by a short laser pulse ($\sim$ 10 ns, resulting in a surface temperature rise of $\Delta T \approx 100$ K of same duration [30]). The correct data analysis affords a measurable residence time of the adspecies of interest on the selected surface, it was estimated to be higher than 1 μs at a temperature of 300 K. Although this residence time is short in comparison to the time scale of fluctuation intervals, it is long enough to evaluate it by fast transient methods. By this method the field dependence of the different surface species (Fig. 7) was obtained from the ToF data (insert in Fig. 7) The unexpected occurrence of O_2 adspecies in the ToF spectrum will be discussed later.

Data in Figure 7 suggest the field of about 15 V/nm for the H_2-oxidation experiments (to avoid considerable oxygen field ionisation respectively desorption). The diversity of the desorbed "water" species in Figure 7 gets clearer, if the field induced reaction routes for the H_2-oxidation according to [52,65] are considered:

$$H_2O_{f-ad} \rightarrow H_2O^+_{gas} + e^-_{Pt} + * \qquad (4.4)$$

$$H_2O_{f-ad} + H_2O_{f-ad} \rightarrow H_3O^+_{gas} + e^-_{Pt} + * + OH_{ad} \qquad (4.5)$$

$$OH_{ad} + OH_{ad} + OH_{ad} \rightarrow H_3O^+_{gas} + e^-_{Pt} + 2O_{ad} \qquad (4.6)$$

$$O_{ad} + O_{ad} \rightarrow O^+_{2\ gas} + 2e^-_{Pt} + 2* \qquad (4.6a)$$

$$H_2O_{f-ad} + H_{ad} \rightarrow H_3O^+_{gas} + e^-_{Pt} + 2* \qquad (4.7)$$

where the subscript $_{f\text{-}ad}$ means "field adsorbed". The rather high dipole moment of the water molecule provides a field induced binding of the order of 0.4 eV to the surface according to FIAES data [61]. Even at a higher reaction temperature the dwell time of this precursor for the routes (4.5) and (4.7) is sufficient for formation of the "volatile" $H_3O_{f\text{-}ad}$ species. Since steps (4.1) to (4.3) are important precursors for the field induced steps (4.4) to (4.7) which occur in a FIM (high positive field), and further on, since the reaction steps (4.1) to (4.3) are relevant only at FEM conditions (negative field of $\sim$0.5 V/Å, no emission of positive ions), a comparison of the FIM and FEM experiments at identical conditions seemed to be mandatory. This was performed as a defined titration reaction starting with an oxygen covered Pt-surface (O_2 exposure of $>$ 1000 L at 10^{-4} mbar) followed by introduction of hydrogen ($4.6 \cdot 10^{-7}$ mbar at 395 K, Figure 8, [52]). In the FEM mode (Figure 8a–d) the disappearance of the O_2-adlayer (dark image, high work function) starts near the (111) planes on the adjacent (331) terraces, the reaction front propagates via the (012) planes towards the central (001) plane, leaving the (011) planes still O_{ad}-covered until the central (001) plane is completely reduced and covered by hydrogen finally. The anisotropic motion of the reaction front is displayed by the switching of the areas from dark to bright, due to the low work function of the clean or (somewhat later) hydrogen covered surface.

In the FIM mode the reaction front can be directly observed (Figure 8e–h) as the bright emission of the H_3O^+ products ions, which are formed according to the field related steps (4.5), (4.6), (4.7). Surprisingly, the same surface sensitivity of the titration reaction is

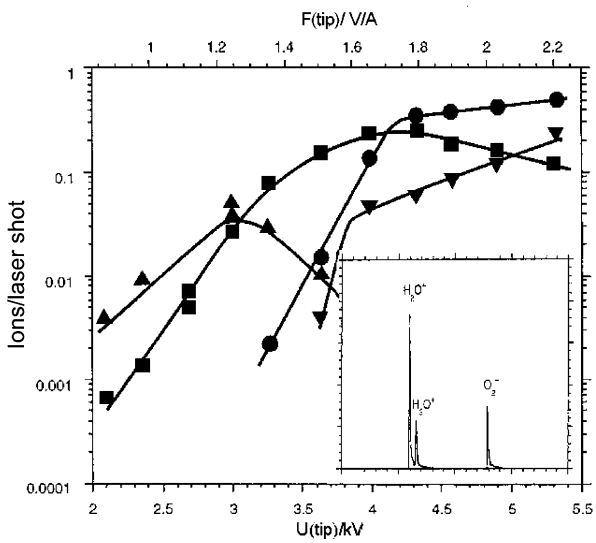

Figure 7. Laser induced field desorption: field dependence of the ion yield for the system H_2O/Pt_{tip} at 300 K and at $p_{H2O} = 2 \cdot 10^{-5}$ mbar, species: ▲ $H_3O \cdot H_2O^+$, ● H_3O^+, ■ H_2O^+, ▼ O_2^+. Insert: ToF-spectrum at 19 V/nm.

observed, the front is again starting from (331), (111) environment and is spreading to the central (001) plane at the same time scale of ca 2 s, only the retarded titration of the (011) planes is not observed.

From these observations we derive a conclusion that for both cases the steps limiting the reaction rate are given by the reaction equation (4.1) to (4.3) and by the preceding adsorption process, or in other words, the field induced routes are very fast in comparison. This insight justifies the FIM investigation in order to get information on the reactive sites which should be same as at field free condition.

At certain conditions the hydrogen oxidation on a Pt tip shows oscillatory kinetic pattern, observed both in FEM and in FIM mode and described in detail in Refs. [52,58]. As a feedback mechanism the reconstruction of the central (100) plane is deduced directly from the FIM images. The cycle of reconstruction of (1×1) and lifting of *hex* structure is discussed in detail in [66], in this context it is noteworthy to remark, that the cycle is connected with a considerable change of density in the top Pt layer which has to eject about 20% of the atoms [67]. This process is combined with formation and dissolution of surface clusters which will be discussed below. The observation of creation and removal of surface aggregates means forming and destroying of the relevant catalytic centres, an observation which goes far beyond the static consideration of active sites once discussed by H. S. Taylor [68].

The fate of such high reactive surface clusters can be followed by observing the reaction with FIM in a nearly steady state on the "oxygen side" near the instability region (Figure 9, [66]). At 430 K the reaction displays a pronounced crystallographic specificity (Figure 9b, c): high brightness (and catalytic activity) is observed mainly in the external regions along the (110) vicinal, where a broad emission area exists. At temperatures of about 430 K an atomic resolution cannot be expected because of the high thermal mobility of reactants which causes momentum transfer to ionic species at the instant of ion formation and because some part of the reaction enthalpy may still present in their kinetic energy [69]. Nevertheless, the central part of the FIM images in Fig. 9 is of particular interest: the dark broad ring limited by the {012}-type planes is probably due to a hydrogen coverage in these areas which are catalytically inactive. Reaction products are formed only at steps around the central (001) plane. In Fig. 9b three bright emitting rings are visible which correspond to the ledges and kink sites around the (001) terraces. The terrace sites of this (001) plane are not imaged at all, that means they are inactive. This example seems to confirm the adlineation model postulated by Schwab [70]; only those sites which are exposed by special crystallographic coordination at ledges and rims [around the (001) plane] are imaged as catalytic sites where the product (mainly H_3O^+) of the catalytic reaction is formed. Apparently the sites in the central (001) plane are not always invisible: the central (001) plane in Fig. 9c shows features which are present only for limited periods (< 200 ms) during the reaction, just when a chemical wave due to a sporadic instability has passed over this area. Small on-top Pt islands are formed, which display a high catalytic activity indicated by their brightness in the FIM. In the (100) area in the micrographs of Fig. 9d–f the details of the further fate of the surface clusters can be observed. In the first step the top (100) face breaks into surface clusters Pt_nO_m, which move incidently to the rim of the underlying terrace where they are incorporated into the ledge. The motion of the "last" cluster at

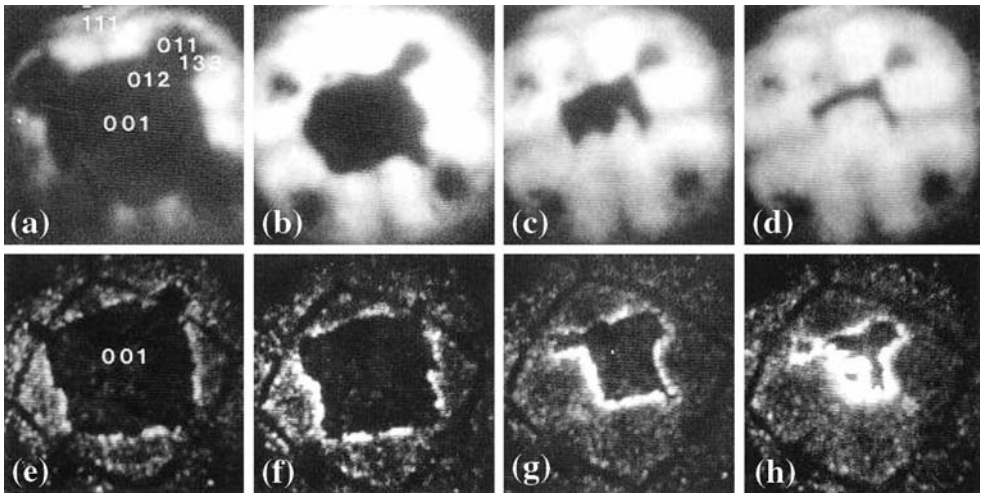

Figure 8. (**a--d**) FEM- and (**e--h**) FIM-images of a Pt tip (r_{tip} = 180 nm) during the titration reaction. The O_{ad} layer (dosing > 1000 L of oxygen) is reacted off at T = 395 K by hydrogen admitted via a pressure jump at $p_{H2} = 4.6 \cdot 10^{-7}$ mbar. In FEM the disappearance of the O_{ad} layer (dark) is accompanied by bright-field emission from the H_{ad} layer; frames are taken at τ-values: (**a**) 0 s, (**b**) 1.0 s, (**c**) 1.3 s, (**d**) 1.4 s. In FIM, in turn, a bright reaction front (H_3O^+ ions) moving from the (331), (111) facets towards the (012) orientations and then towards the central (001) facet ; corresponding τ-values: (**e**) 0 s, (**f**) 0.5 s, (**g**) 1.3 s, (**h**) 1.5 s. Taken from [52].

"5.8 s" was followed by a random walk analysis: after 19 steps over the (100) terrace this aggregate dissolved at "13.3 s". The apparent diffusion constant $D = <\Delta x^2>/4\tau$ amounts 4.2×10^{-15} cm^2/s at 430 K, which is by nearly 100 times lower than for a single Pt-atom on Pt(100) as measured by G. Kellogg [71] and originates from the much bigger size. The original *hex* (100) terrace consists of ~250 Pt atoms, it is clear from the FIM image that the clusters formed are 3-dimensional in shape, but the real size of the Pt_nO_m is not directly accessible by FIM, since the aggregates are acting as micro protrusion emitters.

More is known about their chemical composition. This is accomplished by laser induced FD, the measured ToF-spectrum (not shown) displays besides the water species H_2O_{ad} and H_3O_{ad} the substrate as Pt and the oxides as PtO and PtO_2. Due to the preferential field evaporation of surface clusters, we suggest their partial oxidation. The abundance of these oxidic species depends on temperature and gas pressure but details are still under investigation. Anyway the observed material transport during the ongoing reaction causes morphological changes of the Pt emitter, which manifests itself in a gradual growth of the central (100) plane during reaction.

4.2. Reaction pathways

The kinetics of the $H_2/O_2/Pt$ system is determined by control parameters as T, p_{O2}, and p_{H2}. Keeping T and p_{O2} constant and changing p_{H2} cyclewise a pronounced hysteresis of the H_3O^+ products ion yield is observed (Fig. 10a, [65]): the total ion yield (mainly H_3O^+) increases until it reaches a critical value $p_{crit.low}$ where the regimes switches into bistability. By further increase at an upper critical pressure $p_{crit.high}$ the reaction yield

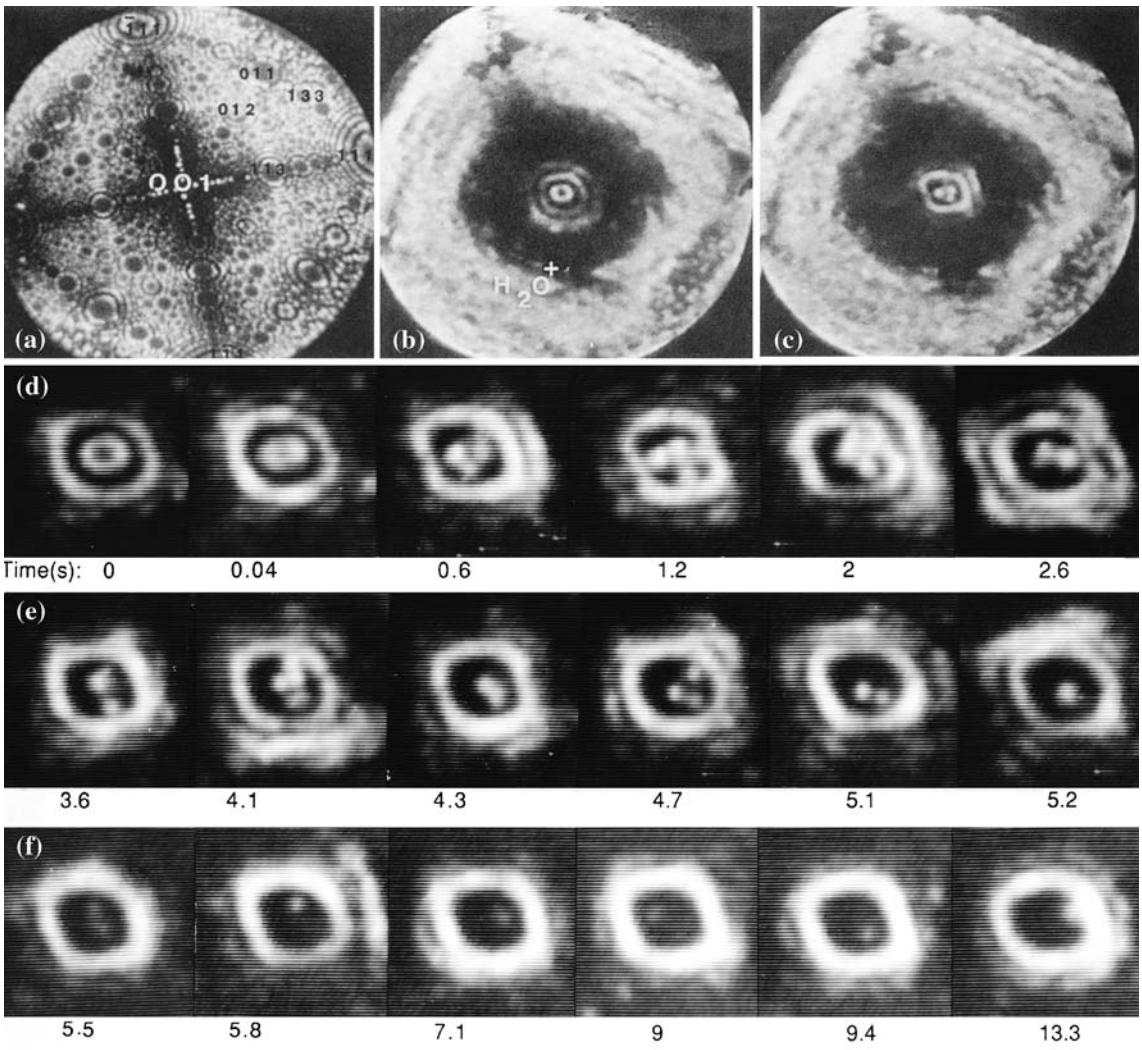

Figure 9. Mobile high reactive surface clusters on Pt. (**a**) Clean apex surface of a [001]-oriented Pt tip imaged by Ne^+ ions at 78 K (r_{tip} = 70 nm, $p_{Ne} = 2\cdot10^{-4}$ mbar, F_0 = 45 V/nm, Miller indices indicate the facet orientation). (**b**) H_2 oxidation *in situ* imaged at 430 K, $p_{H2} = 7\cdot10^{-4}$ mbar, $p_{O2} = 5\cdot10^{-4}$ mbar. The imaging ions are predominantly H_3O^+ as a reaction product, F_0 = 15 V/nm. (**c**) the same, but 0.6 s later, after the reaction wave has passed the central (001) plane (**d--f**) a magnified view on the central (001) facet: sequence of video frames. Taken from [66].

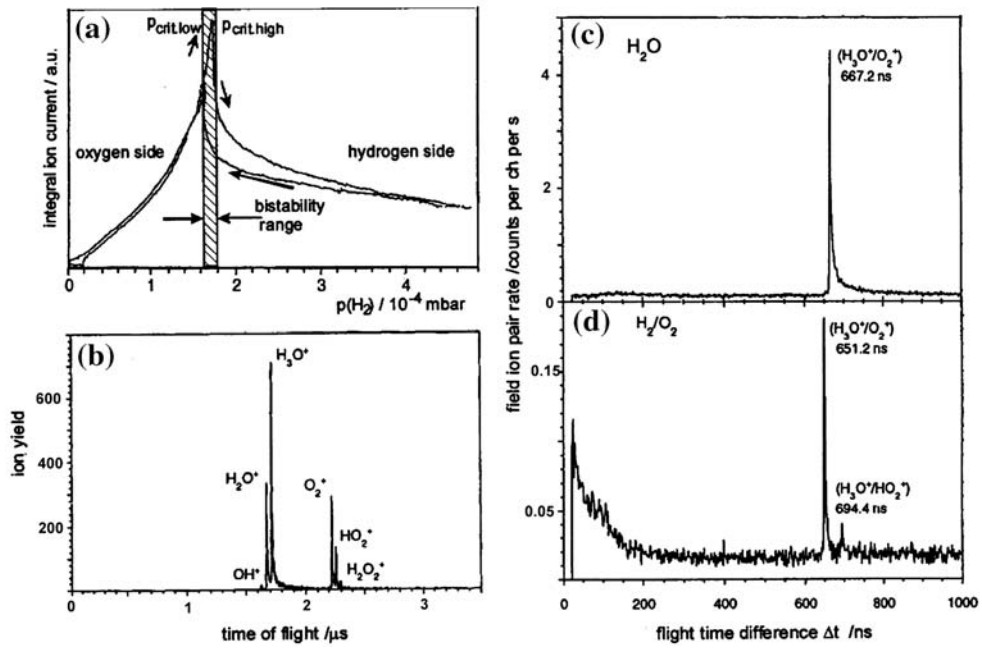

Figure 10. (**a**) Hysteresis in the hydrogen oxidation reaction rate, $p_{O_2} = 3.6{\cdot}10^{-4}$ mbar, T = 413 K. (**b**) Pulsed laser induced field desorption during reaction, $p_{O_2} = 2.2\times10^{-4}$ mbar, $p_{H_2} = 1.10^{-4}$ mbar, T = 400 K. (**c**) Time correlation of H_2O^+ field ions, $p = 8\,10^{-5}$ mbar, T = 300 K. (**d**) Field ion correlation for O_2/H_2-reaction, "oxygen side", $p(H_2) = 1.35\times10^{-4}$ mbar, $p_{O2} = 10^{-4}$ mbar, T = 430 K. Taken from [65].

drops in a kinetic phase transition and is further reduced with higher p_{H2} due to poisoning effects on the "hydrogen side". Within the bistability region pronounced fluctuations and periodic oscillations are observed. A hysteresis behaviour can be observed also with FEM but as somewhat less pronounced. The similar scenario was observed on a polycrystalline Pt foil [72], what favours a conclusion that the neighbouring low index nanofacets are essential for the bistability since on the single Pt crystals this could not be observed. We note, that on the oxygen side H_3O^+ is formed according to step (4.6) with A = 10.4 eV (slow) on the hydrogen side according to step (4.7) with A = 9.2 eV (fast).

To get access to a chronological linkage between the different reaction steps a correlation experiment was performed [65]. According to the reaction (4.5) followed by step (4.3) we have tested the correlated emission of ions like: H_3O^+ and O^+ or $H_2O^+$and O^+ or the two water species $H_3O^+$and H_2O^+, for both reaction systems: H_2O/Pt and H_2/O_2/Pt. It turned out that all these emission events were statistically independent of each other on a time scale of ns.

A correlated emission of H_3O^+ and of O_2^+, was observed in turn for the system H_2O/Pt (Figure 10c): the sharp peak at 667.2 ns on top of randomized pair events rate exactly corresponds to the difference of flight times (Δt_f) of these ions known from pulsed laser FD experiments. In corresponding measurements during ongoing H_2 oxidation, the same correlation (Fig. 10d) is observed at the oxygen side of the reaction. The tailing of the correlation peak is less developed, and a small additional peak can be identified as the simultaneous emission of H_3O^+ and HO_2^+. Within the experimental error the coincidence of emission of H_3O^+ and O_2^+ occurs from the selected sites within less than 100 ps (measured with time-amplitude converters). Therefore, we conclude that the H_3O^+ and O_2^+ species are originating from the same transition complex. To get an indication of its nature, we analyzed the pulsed laser field desorption spectrum, as obtained during H_2/O_2 reaction (Fig. 10b). The minority species are identified as OH^+, HO_2^+ and $H_2O_2^+$, which were also detected in the water FD spectrum by Schmidt [64]. The peroxy complex H_2O_2 as an intermediate in H_2 oxidation has been already proposed by Verheij et al. [73] who investigated the reaction on Pt(111) by modulated molecular beam transient spectroscopy.

Field adsorbed water agglomerates even at room temperature at the surface, as expressed by the emission of protonated water cluster ions as a minority route, and as well by the formation of H_3O^+ from two water molecules in step (4.5) and not by the energetically more favored direct protonation, as is prevailing at the hydrogen side of the reaction or also for the H_2/H_2O/Pt system [61]. From these findings we conclude that the hydroxyls are formed in close vicinity, and that the peroxy complex emerges from two OH_{ad}. We explain simultaneous emission of H_3O^+ and O_2^+ for the studied reaction systems by the following disproportionation:

$$OH_{ad} + (OH_{ad}\cdot\cdot OH_{ad}) \rightarrow H_3O^+_{gas} + O^+_{2\ gas} + 2e^-_M \quad (4.6b)$$

This should not be misinterpreted as a triple collision (H_2O is also formed in successive steps from H_{ad}, H_{ad} and O_{ad}). By changing the probe hole position, we found out that only the reactive sites (bright in FIM image) emitted H_3O^+ and O_2^+ simultaneously; the nature of these sites is still obscure. If the reaction switches to the hydrogen side (just by increasing p_{H2}), no correlation is detected any more, in agreement with the observed protonation of H_2O by hydrogen as discussed in Ref. [60].

Resuming the interpretation of the simultaneous ion emission events, a formation of O_2^+ from two "hot" O_{ad} may be conceived alternatively. "Hot" means that a fraction of the reaction enthalpy is released as kinetic energy of O_{ad}. For FD of pure water, O_{ad} can be exclusively produced by step (4.3). An H_2O_{ad} may react immediately with an adjacent one according to reaction (4.5) involving FD of H_3O^+. The OH_{ad} may be attached to an O_{ad} to form the minority species HO_2^+ as observed in Fig. 10b. Raising the temperature from 300 to 400 K for the H_2O/Pt system the emission of the ion pair H_3O^+, HO_2^+ is also detected (Fig. 10c). If O_2^+ would emerge from a fragmentation of HO_2^+, one cannot explain the observability of HO_2^+ in the coincidence spectrum appearing only above 400 K.

A direct formation of O_2^+ from hot O_{ad} with a minimum of steps can be conceived by the following: two H_2O_{ad} are produced adjacently according (4.3) from four hydroxyls, and then the O_{ad} recombine. At the same instant H_3O^+ could be formed by the disproportionation (4.4). If H_3O^+ and O_2^+ were formed in individual steps each, then the tailing of the coincidence spectra would be symmetric in time. But only a delay for O_2^+ emission is observed in the peak. If this model is correct, the H_2O diffusion forming the water dimer and the disproportionation in sequence would be very fast compared to the recombination of the two "hot" O_{ad} within of some hundred picoseconds.

It has to be stressed that the correlated formation of O_2^+ and H_3O^+ seems to be only a minority route, about 90% of the O_2^+ appear as uncorrelated (as derived from an analysis of the statistical background in Fig. 10c). For these ions a formation from thermally equilibrated O_{ad} is not possible at these temperatures, but as indicated before, "hot" O species according to step (4.3) may be conceived. At least during H_2/O_2 reaction, the sum of the emitted H_2O^+ appear to carry up to 0.6 eV translational surplus energy with it, as the appearance energy data show [61].

In conclusion to this chapter, the reaction pathways leading to an O_2^+ abundance in the field ion spectrum of the H_2O-Pt and the H_2/O_2-Pt system are a consequence of the preferential H_3O^+ emission under field conditions due to the proportionation reaction of two adjacent H_2O molecules. A peroxy intermediate or a recombination of non-equilibrated O species are proposed as precursors.

5. Resumé

In situ microscopic and spectroscopic studies on carbon monoxide respectively hydrogen oxidation on various facets of nm-sized platinum tips demonstrate that the catalytic properties of differently oriented Pt nanofacets assembled to a complex reaction system can be effectively studied using the field-emission based techniques. The findings gained in our experiments for the well defined heterogeneous Pt surfaces (characterized with atomic resolution) demonstrate that resulting properties of such a heterogeneous system as an apex of a field emitter tip (or a Pt pellet of a supported catalyst) cannot be regarded just as a kind of a superposition of the reactivity of the corresponding crystal planes. To explain the spatio-temporal behaviour of a catalytic reaction in such a complex nanosystem one has not only to consider the local coupling between diffusion and reactivity on the adjacent nano-facets, but also the influence of the atomic steps confining the individual nanofacets and attenuating this coupling as well as to take into account the prominent role of the fluctuation effects. The FEM with its resolution of ~2 nm and the FIM with atomic resolution appear to be well suitable techniques for *in situ* studying fluctuations: the "parallel" imaging principle of the FEM/FIM makes it possible to analyse simultaneously the processes on the different surface regions. Processing of the digitized video-sequences allow to study the reaction dynamics within regions of interest of few nm^2 arbitrarily located on the surface with a time resolution limited just by the used video-technique. The electrostatic field of ca 5 V/nm applied in FEM does not influence neither the CO oxidation nor H_2 oxidation on Pt, the significantly higher field of ca 10 V/nm (and of an opposite direction) in FIM influences though both of these reactions, the study of the field effect allows, however, to reveal the effects of the electron density redistribution on the surface (important for the understanding of the promoters effect) and (via influencing the surface diffusion) to study the details of the propagation of "chemical waves" and of the diffusive coupling.

The resulting changes in the surface topography caused by the ongoing reaction can be visualized with atomic resolution and the atomic-scale mechanisms, such as motion of the nanosized 3D-aggregates (e.g. Pt-clusters on a Pt(100) facet during H_2 oxidation leading to the surface coarsening), can be studied *in situ* by FEM/FIM techniques.

Recapitulatory, it has to be noted, that although the FIM and related microscopies are the oldest techniques that provide the ultimate lateral resolution of the imaged structures (atomic FIM imaging turns 50 these days [23]), the capacity of the field emission based microscopies in the catalytic research is by far not adequately utilised yet. Atomic scale tuning of the single catalytic particles, external control of the bifurcation

points and of the whole kinetic phase diagram of a surface reaction by the particle size and shape, as well as by the applied electric field are just few points indicating the potential of this approach to the nanometer scale catalysis.

References

[1] H.-J. Freund, N. Ernst, T. Risse, H. Hamann and G. Rupprechter, Phys. Stat. Sol.(a) 187 (2001) 257.
[2] H.-J. Freund, Surf. Sci. 500 (2002) 271.
[3] D.W. Googman, J. Catal. 216 (2003) 213.
[4] M. Laurin, V. Johánek, A.W. Grant, B. Kasemo, J. Libuda and H.-J. Freund, J. Chem. Phys. 122 (2005) 084713.
[5] G. Rupprechter, K. Hayek, L. Rendon and M. Jose-Yacaman, Thin Solid Films 260 (1995) 148.
[6] A.S. Eppler, G. Rupprechter, L. Guczi and G.A. Somorjai, J. Phys. Chem. B101 (1997) 9973.
[7] Y. Suchorski, J. Beben, E.W. James, J.W. Evans and R. Imbihl, Phys. Rev. Lett. 82 (1999) 1907.
[8] H.-J. Freund, M. Bäumer, J. Libuda, H. Kuhlenbeck, K. Al-Shamery and H. Hamann, Cryst. Res. Technol. 33 (1998) 977.
[9] http://www.fhi-berlin.mpg.de/th/personal/hermann/pictures.html.
[10] Y. Suchorski, W.A. Schmidt and J.H. Block, Appl. Surf. Sci. 67 (1993) 124.
[11] V.V. Gorodetski, W. Drachsel and J.H. Block, Catal Lett. 19 (1993) 223.
[12] V.K. Medvedev, Y. Suchorski and J.H. Block, Surf. Sci. 343 (1995) 169.
[13] C. Voss and N. Kruse, Appl. Surf. Sci. 87/88 (1995) 127.
[14] V.K. Medvedev, Y. Suchorski, C. Voss, T. Visart de Bocarme, T. Bär and N. Kruse, Langmuir 14 (1998) 6151.
[15] K. Hayek, M. Fuchs, B. Klötzer, W. Reichl and G. Rupprechter, Top. Catal. 13 (2000) 55.
[16] V.V. Gorodetski, J.H. Block, W. Drachsel and M. Ehsasi, Appl. Surf. Sci. 67 (1993) 198.
[17] V.V. Gorodetski and W. Drachsel, Appl. Catal. A: General 188 (1999) 267.
[18] V.K. Medvedev and Y. Suchorski, Surf Sci Lett 364 (1996) L540.
[19] V.V. Gorodetskii, V.I. Elochin, J.W. Bakker, B.E. Nieuwenhuys, Cat.Today 105 (2005) 183, and references therein.
[20] T.T. Tsong, *Atom-Probe Field Ion Microscopy* (Cambridge University Press, Cambridge, 1990).
[21] W.A. Schmidt, Y. Suchorski, J.H. Block, H.J. Kreuzer and R.L.C. Wang, Surf. Sci. 326 (1995) 243.
[22] V. Gorodetskii, N. Ernst, W. Drachsel and J.H. Block, Appl. Surf. Sci. 87/88 (1995) 151.
[23] E.W. Müller and K. Bahadur, Phys. Rev. 102 (1956) 634.
[24] I.V. Goldenfeld, I.Z. Korostyshewsky and B.G. Mischanchuk, Intern. Mass. Spectrom. Ion. Phys. 13 (1974) 297.
[25] R.G. Forbes, Surf. Sci. 61 (1976) 221.
[26] N. Ernst, Appl. Surf. Sci. 67 (1993) 82.
[27] B. Sieben, Y. Suchorski, G. Bozdech, N. Ernst and Z. Physik, Chem. 202 (1997) 103.
[28] W. Drachsel and J.H. Block, Surf. Sci. 246 (1991) 141.
[29] J.H. Block, J. Dirks and W. Drachsel, Rev. Eat. Met. Mat. 11 (1992) 39.
[30] W. Drachsel, Th. Jentsch and J.H. Block, Int. J. Mass. Spec. Ion Phys. 46 (1983) 293.
[31] I. Langmuir, Trans. Faraday Soc 17 (1921) 621.
[32] T. Engel and G. Ertl, J. Chem. Phys. 69 (1978) 1267.
[33] M. Bär, C. Zülicke, M. Eiswirth and G. Ertl, J. Chem. Phys. 96 (1992) 8595.
[34] R.M. Ziff, E. Gullari and Y. Barshad, Phys. Rev. Lett. 56 (1986) 2553.
[35] F. Zhang, D.Y. Hua and Y.-Q. Ma, J. Phys. Condens. Matter 14 (2002) 10093.
[36] G. Ertl, Adv. Catal. 45 (2000) 1, and references therein.
[37] Y. Suchorski, R. Imbihl and V.K. Medvedev, Surf. Sci. 401 (1998) 392.
[38] Y. Suchorski, Ultramicroscopy 73 (1998) 139.
[39] M. Eiswirth, P. Möller, K. Wetzel, R. Imbihl and G. Ertl, J. Chem. Phys. 90 (1989) 510.
[40] S. Moldenhauer, PhD Thesis, Freie Universität, Berlin, 1996.
[41] K.D. Rendulic and M. Leisch, Surf. Sci. 93 (1980) 1.
[42] K.D. Rendulic and M. Leisch, Surf. Sci. 95 (1980) L271.
[43] Y. Suchorski, W.A. Schmidt, N. Ernst, J.H. Block and H.J. Kreuzer, Prog. Surf. Sci. 48 (1995) 121.
[44] Y. Suchorski and J. Beben, Prog. Surf. Sci. 74 (2003) 3.
[45] Y. Suchorski, J. Beben, H. Weiss, Symposium on Surface Science 3S'04, St. Christoph am Arlberg, Austria, Contributions, Eds. F. Aumayr and P.Varga, p. 145.
[46] Y. Suchorski, J. Beben, A. Frac, V.K. Medvedev, H. Weiss, Surf. Interface Anal., 39 (2007) 161.
[47] Y. Suchorski, J. Beben and R. Imbihl, Surf. Sci. 454/456 (2000) 331.
[48] K. Fichthorn, E. Gulari and R.M. Ziff, Rhys. Rev. Lett. 63 (1989) 1527.
[49] Y. Suchorski, J. Beben, R. Imbihl, E.W. James, Da-Jiang Liu and J.W. Evans, Phys. Rev. B 63 (2001) 165417.
[50] Y. Suchorski, J. Beben and R. Imbihl, Prog. Surf. Sci 59 (1998) 343.
[51] V. Johánek, M. Laurin, A.W. Grant, B. Kasemo, C.R. Henry and J. Libuda, Science 304 (2004) 1639.
[52] V. Gorodetskii, J.H. Block and W. Drachsel, Appl. Surf. Sci. 76/77 (1994) 129.
[53] P.R. Norton, in "The Chemical Physics of Solid Surfaces and Heterogeneous Catalysis", D.A. King and Woodruff D.P., Eds. (Elsevier, Amsterdam, 1982) Vol. 4, p. 27.
[54] V.J. Kwasniewski and L.D. Schmidt, J. Chem. Phys. 96 (1992) 5931.
[55] D.F. Padowitz and S.J. Sibener, Surf. Sci. 254 (1991) 125.
[56] A.B. Anton and B.C. Cadogan, Surf. Sci. 239 (1990) L548.
[57] B. Hellsing, B. Kasemo and V.P. Zhdanov, J. Cat. 132 (1991) 210.
[58] J.H. Block, W. Drachsel, N. Ernst, B. Sieben and V. Gorodetskii, Ber. Bunsenges. Phys. Chem. 99 (1995) 1363.
[59] V. Gorodetskii, J. Lauterbach, H.H. Rotermund, J.H. Block and G. Ertl, Nature 370 (1994) 276.
[60] B. Sieben, G. Bozdech, N. Ernst and J.H. Block, Surf. Sci. 352 (1996) 167.
[61] B. Sieben, G. Bozdech and N. Ernst, J. de Physique IV 6-C5 (1996) 5.
[62] Y. Suchorski, W.A. Schmidt, N. Ernst and J.H. Kreuzer, Prog. Surf. Sci. 48 (1995) 121.
[63] H.D. Beckey, Z. Naturforsch, Teil A 14 (1959) 712.
[64] W.A. Schmidt, Z. Naturforsch, Teil A 19 (1964) 318.
[65] W. Drachsel, C. Wesseling and V. Gorodetskii, J. de Physique IV 6-C5 (1996) 31.
[66] J.H. Block, V. Gorodetskii and W. Drachsel, Recl. Trav. Chim. Pays-Bas 113 (1994) 444.
[67] K. Heinz, E. Lang, K. Strauss and K. Müller, Appl. Surf. Sci. 11/12 (1982) 611.
[68] H.S. Taylor, Proc. Royal Soc. London (A) 108 (1925) 105.
[69] B. Hellsing, B. Kasemo and V.P. Zhdanov, J. Catal. 132 (1991) 210.
[70] G.M. Schwab and E. Pietsch, Z. phys. Chem. B1 (1929) 385.
[71] G.L. Kellogg, Surf. Sci. 246 (1991) 31.
[72] M.M. Slin'ko, N.I. Jaeger, in Oscillating Heterogeneous Catalytic Systems" in Surface Science and Catalysis 86, Edit. B. Delmon and J. T. Yates (Elsevier, Amsterdam 1994), p. 131.
[73] E.K. Verheij, M. Freitag, M.B. Hugenschmidt, I. Kempf, B. Poelsema and G. Comsa, Surf. Sci. 272 (1992) 276.